



Silica and zirconia supported catalysts for the low-temperature ethanol steam reforming

Ilenia Rossetti^{a,*}, Josè Lasso^a, Valentina Nichele^b, Michela Signoretti^b,
Elisabetta Finocchio^c, Gianguido Ramis^c, Alessandro Di Michele^d

^a Dip. di Chimica, Università degli Studi di Milano, INSTM Unit Milano-Università and CNR-ISTM, via C. Golgi, 19, I-20133 Milano, Italy

^b Dip. di Scienze Molecolari e Nanosistemi, Università Ca' Foscari Venezia and INSTM Unit Venezia, Calle Larga S. Marta, 2137 Venezia, Italy

^c Dip. di Ingegneria Civile, Chimica e Ambientale, Università degli Studi di Genova and INSTM Unit Genova, P.le J.F. Kennedy 1, I-16129 Genova, Italy

^d Dip. di Fisica, Università degli Studi di Perugia, Via Pascoli, 06123 Perugia, Italy

ARTICLE INFO

Article history:

Received 14 October 2013

Received in revised form 4 December 2013

Accepted 6 December 2013

Available online 17 December 2013

Keywords:

Ethanol steam reforming

H₂ production

Ni catalysts

Silica

Zirconia

Catalyst deactivation

Coking

ABSTRACT

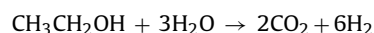
Ethanol steam reforming has been investigated in the low temperature range, focusing not only on H₂ productivity, but also on catalyst stability, very critical parameters under such conditions. Different supports (SiO₂ and ZrO₂), active phases (Ni, Co, Cu) and reaction temperature (300–500 °C) have been employed. Ni confirmed the best performing active phase to promote ethanol decomposition and reforming already at low reaction temperature. However, stability towards coking remains a key problem. The support plays a key role from this point of view. Indeed, the stabilization of the active phase in very dispersed form allowed to reach stable catalyst performance with time-on-stream. SiO₂, thanks to no Lewis acidity and sufficiently strong metal–support interaction, demonstrated an interesting support for Ni under the selected operating conditions.

© 2013 Elsevier B.V. All rights reserved.

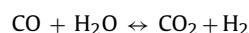
1. Introduction

The steam reforming of ethanol raised interest for the production of H₂ from a renewable source. Broad efforts have been devoted to develop active and stable catalytic systems for this application. Among non noble metal catalysts Ni and Co exhibited the most interesting performance, suggesting to optimize their formulation to achieve better results [1–9].

The steam reforming process is composed of many different possible reactions [9], of which we may summarize the most relevant as follows:



which may be seen as the sum of the syngas production and the water gas shift (WGS) reaction:



The latter is exothermal, in contrast to the former. Therefore, when operating under the typical steam reforming conditions the WGS reaction is often at equilibrium. Its degree of advancement may be deduced from the CO/CO₂ ratio.

Ethanol may be dehydrogenated to acetaldehyde, which can be further reformed. However ethanol may also undergo dehydration to form ethylene that can then polymerize to form carbonaceous deposits over the catalyst. Depending on the operating conditions other parasitic reactions induce coke formation, such as CO disproportion (Boudouard reaction), active at moderate temperature, or the decomposition of hydrocarbons, active at high temperature.

Differently prepared Ni-, Co- and Cu-based catalysts supported over TiO₂ have been recently tested for the steam reforming of ethanol. The results evidenced that the highest activity may be reached in general with Ni as active phase, but its tendency to form C filaments remains a key problem, besides possible coking due to support acidity [10–14]. It was also underlined that the interaction strength between the support and the active phase, tunable with the preparation procedure, determines the success of a formulation. For instance, the same 10 wt% Ni/TiO₂ sample was completely inactive when the support was calcined at 500 °C, whereas it was conveniently active and stable when calcined at 800 °C [12–14].

In addition, Ni proved much more stable against coking when prepared in very dispersed form also for the SR of CH₄ [15–18]. The

* Corresponding author. Tel.: +39 0250314059; fax: +39 02 50314300.

E-mail address: ilenia.rossetti@unimi.it (I. Rossetti).

possibility to disperse (and stabilize in dispersed way) the metal depends on the preparation method, but also on the support. ZrO_2 and SiO_2 demonstrated interesting supports for Ni, provided the right preparation route is chosen [12,13]. Therefore, in this work we investigated different Ni-, Co- and Cu-based catalysts supported over ZrO_2 or SiO_2 . In particular a mesoporous SBA-15 support was chosen, trying at least the partial confinement of the active phase into the mesoporous framework. On the other hand, the mean pore size of SBA-15 is much larger than the kinetic diameter of ethanol, so that no significant mass transfer limitations are expected during the reaction.

All the samples were calcined at 500 °C in order to keep the active phase as dispersed as possible and we focused on low temperature activity testing in the temperature range 300–500 °C. Indeed, the possibility to operate at relatively low temperature, i.e. at 500 °C or below, is very attractive to limit the energy input to the reactor. Nevertheless, coking activity is particularly high in such a temperature range, especially with Ni-based catalysts.

In previous investigations [12–14] we managed the coking item by high temperature operation (500–750 °C), so to favour the gasification of the coke deposits in case formed. On the contrary, in the present work we focused on the optimization of metal dispersion and its interaction with the support to improve catalyst stability towards coking. This approach was successfully applied also with Pt-supported samples in this application [19]. Extensive characterization by means of various techniques of both the fresh and spent samples allowed to compare the main physical–chemical properties of the catalysts and to comment activity/stability data.

2. Experimental

2.1. Catalyst preparation

2.1.1. Support synthesis

The SBA-15 support was synthesized as previously reported [20,21], in the presence of Pluronic 123 (P123, Aldrich) as structure directing agent and calcined at 500 °C.

$\text{Zr}(\text{OH})_4$ was prepared by a conventional precipitation method [21,22] at a constant pH of 10.

2.1.2. Addition of the active phase

The active phase was added to each support by incipient wetness impregnation with an aqueous solution of the metallic precursor ($\text{Ni}(\text{NO}_3)_2 \cdot 6\text{H}_2\text{O}$, Sigma Aldrich, purity $\geq 98.5\%$; $\text{Co}(\text{NO}_3)_2 \cdot 6\text{H}_2\text{O}$ Sigma-Aldrich, puriss. p.a. ACS reagent; $\text{Cu}(\text{NO}_3)_2 \cdot 3\text{H}_2\text{O}$ Sigma-Aldrich, puriss. p.a.), in the proper concentration in order to obtain 10 wt% nominal metal loading. The catalyst was dried overnight at 110 °C and then calcined at 500 °C for 4 h.

Catalysts were labelled with a S or Z symbol, referring to SiO_2 or ZrO_2 carriers, respectively, followed by a symbol indicating the metal constituting the active phase (Ni, Co or Cu).

2.2. Characterization

The actual metal concentration in the catalysts was determined by atomic absorption spectroscopy (AA) measurements on a Perkin Elmer AAnalyst instrument after dissolution of the sample.

X-ray powder diffraction (XRD) analysis of the as prepared samples was performed in order to identify the crystalline phases. XRD patterns were collected on a Bruker D8 Advance diffractometer equipped with a $\text{Si}(\text{Li})$ solid state detector (SOL-X) and a sealed tube providing $\text{Cu K}\alpha$ radiation. Phase recognition was possible by comparison with literature data [23].

Specific surface area and pores size distribution were evaluated through N_2 adsorption–desorption isotherms at -196°C

(Micromeritics, ASAP 2000 Analyser). Surface area was calculated on the basis of the BET equation [24], whereas the pores size distribution was determined by the BJH method [25], applied to the N_2 desorption branch of the isotherm. Prior to the analysis the sample was dried overnight at 110 °C and then outgassed at the same temperature for 2 h.

The TPR technique was employed to identify different metallic species possibly present in the catalysts according to the different reduction temperatures, in case used to assess the interaction strength between the active phase and the support. The catalyst was placed in a quartz reactor and heated by $10^\circ\text{C}/\text{min}$ from *r.t.* to 800 °C in a 5% H_2/Ar mixed gas stream flowing at 40 mL/min. TPO analysis was performed by feeding 40 mL/min of a 10 vol% mixture of O_2/He while heating by $10^\circ\text{C}/\text{min}$ up to 650 °C.

SEM images have been obtained using a Field Emission Gun Electron Scanning Microscopy LEO 1525, after metallization with Cr. Elemental composition was determined using Bruker Quantax EDS.

TEM images have been obtained using a Philips 208 Transmission Electron Microscope. The samples were prepared by putting one drop of an ethanol dispersion of the catalysts on a copper grid pre-coated with a Formvar film and dried in air.

FT-IR spectra have been recorded in static conditions by a Nicolet Nexus Fourier transform instrument, using conventional IR cells connected to a gas manipulation apparatus. Pressed disks of pure catalyst and support powders (~ 30 mg) were reduced in the IR cell by heating in pure H_2 at 500 °C and following outgassing at the same temperature. CO adsorption experiments have been performed at -140°C , recording spectra upon warming.

Pivalonitrile (PN, Aldrich, pur. 98%) adsorption experiments have been performed over the reduced samples at room temperature and following outgassing at increasing temperatures.

Skeletal spectra have been recorded in air, after dilution of the catalyst powder with KBr (Aldrich, FT-IR grade) (0.1%, w/w).

Micro-Raman sampling was made by an OLYMPUS microscope (model BX40) connected to an ISA Jobin–Yvon model TRIAX320 single monochromator, with a resolution of 1 cm^{-1} . The source of excitation was a Melles Griot 25LHP925 He–Ne laser that was used in single line excitation mode at $\lambda = 632.8\text{ nm}$. The power focused on the samples was always less than 2 mW. The scattered Raman photons were detected by a liquid-nitrogen cooled charge coupled device (CCD, Jobin–Yvon model, Spectrum One).

UV–vis, NIR spectra of catalyst pure powders have been recorded in air, by a Jasco 570V instrument equipped with a DR cell.

2.3. Activity testing for ethanol steam reforming (ESR)

Details on the equipment for activity testing have been previously reported elsewhere [12]. The catalysts (*ca.* 0.5 g, 0.15–0.25 mm particle size) were diluted 1:3 (vol/vol) with SiC of the same size. The catalyst was activated in 50 cm^3/min of a 20% H_2/N_2 gas mixture, while heating by $10^\circ\text{C}/\text{min}$ up to 500 °C for 1 h.

Activity testing was carried out by feeding 0.017 cm^3/min of a 3:1 (mol/mol) $\text{H}_2\text{O}:\text{CH}_3\text{CH}_2\text{OH}$ liquid mixture by means of a Hitachi, model L7100, HPLC pump, added with 56 cm^3/min of N_2 , used as internal standard, and 174 cm^3/min of He. Such dilution of the feed stream was calibrated so to keep the reactants mixture in the vapour phase even at zero conversion at the reactor outlet.

The activity tests were carried out at atmospheric pressure, GHSV = 1750 h^{-1} (referred to the ethanol + water gaseous mixture) at 500 °C.

The analysis of the out-flowing gas was carried out by GC analysis. Repeated analyses of the effluent gas were carried out every hour and the whole duration of every test at each temperature was *ca.* 8 h. The raw data, expressed as mol/min of each species

Table 1
Main physical–chemical properties of the catalysts.

Sample	Preparation method	Ni, Co, Cu (wt%) ^a	SSA (m ² /g) ^b	Mean pore size (nm)	Crystal size (nm) ^c
S–Ni	Ni/SiO ₂ (SBA-15) calcined at 500 °C	9.2	709	6.3	16
Z–Ni	Ni/ZrO ₂ calcined at 500 °C	9.7	158	10.1	5
S–Co	Co/SiO ₂ (SBA-15) calcined at 500 °C	7.8	629	6.4	6
S–Cu	Cu/SiO ₂ (SBA-15) calcined at 500 °C	6.8	672	6.2	39

^a From atomic absorption analysis.

^b SSA, specific surface area, from BET model.

^c Crystal size determined by Rietveld analysis on the reduced catalyst.

outflowing from the reactor, averaged after 4–8 h-on-stream, have been elaborated as follows:

Products distribution:

$$Y_i = \text{mol } i / \Sigma(\text{mol } i)$$

C balance:

$$100 - \frac{(\text{mol CH}_3\text{CH}_2\text{OH} \times 2)_{\text{in}} - \Sigma(\text{mol } C_i \times \chi_i)_{\text{out}}}{(\text{mol CH}_3\text{CH}_2\text{OH} \times 2)_{\text{in}}} \times 100$$

Conversion:

$$X_i = \frac{\text{mol } i_{\text{in}} - \text{mol } i_{\text{out}}}{\text{mol } i_{\text{in}}} = \text{H}_2\text{O}, \text{CH}_3\text{CH}_2\text{OH}$$

Selectivity:

$$S_i = \frac{\text{mol } i / \nu_i}{\text{mol ethanol}_{\text{in}} - \text{mol ethanol}_{\text{out}}}$$

H₂ yield:

$$\text{Yield} = X_{\text{ethanol}} \times S_{\text{H}_2} = \frac{\text{mol H}_2}{\nu_{\text{H}_2}} \times \text{mol ethanol}_{\text{in}}$$

H₂ productivity:

$$\frac{\text{mol H}_2 \text{ out}}{\text{min kg}_{\text{cat}}}$$

where i , products detected, dry basis; χ_i , number of C atoms in the i th molecule; ν_i , stoichiometric coefficient of species i in the ESR reaction.

3. Results and discussion

3.1. Textural, structural and morphologic properties

The main physical chemical properties of the prepared catalysts are reported in Table 1.

SBA-15-supported samples showed very high surface area. In particular, they were characterized by a IV-type isotherm with a H1-type hysteresis. This is typical of this support, which is a mesoporous material with a high surface area ($\approx 700 \text{ m}^2/\text{g}$) and a sharp pores size distribution, with a maximum located at *ca.* 6 nm. Sample Z–Ni exhibited a IV-type isotherm containing a H3-type hysteresis, typical of materials that do not possess a well-defined mesoporous structure.

The TPR technique was employed to identify the different species present in the catalysts according to the different reduction temperatures. Moreover, this technique allows to qualitatively assess the existence and strength of metal/support interactions. Indeed, the TPR technique has been commonly used since long years ago to investigate the existence and intensity of metal–support interaction (see e.g. [26–28]). The lower the reducibility, the stronger the metal–support interaction. Very dispersed particles more strongly interact with the support, thus, for a given metal more dispersed particles and/or more strongly interacting with the support usually reduce at higher temperature.

The TPR profile of sample S–Ni is reported in Fig. 1a. This sample gave rise to a rather broad reduction feature in the range 300–500 °C. A well-defined peak with its maximum at 390 °C was indeed detected, with a shoulder between 300 and 360 °C and another one between 420 and 500 °C, indicating that different NiO species were present on the support.

Also the TPR profile of Z–Ni (Fig. 1b) suggests the existence of three different NiO species on the zirconia surface (three different peaks at 280 °C, 380 °C and 520 °C), whereas the bare ZrO₂ did not evidence any reduction peak.

According to the pertinent literature [29–32], the peak located at the lowest temperature is ascribable to metal oxide particles very poorly interacting with the support. It is reported that unsupported

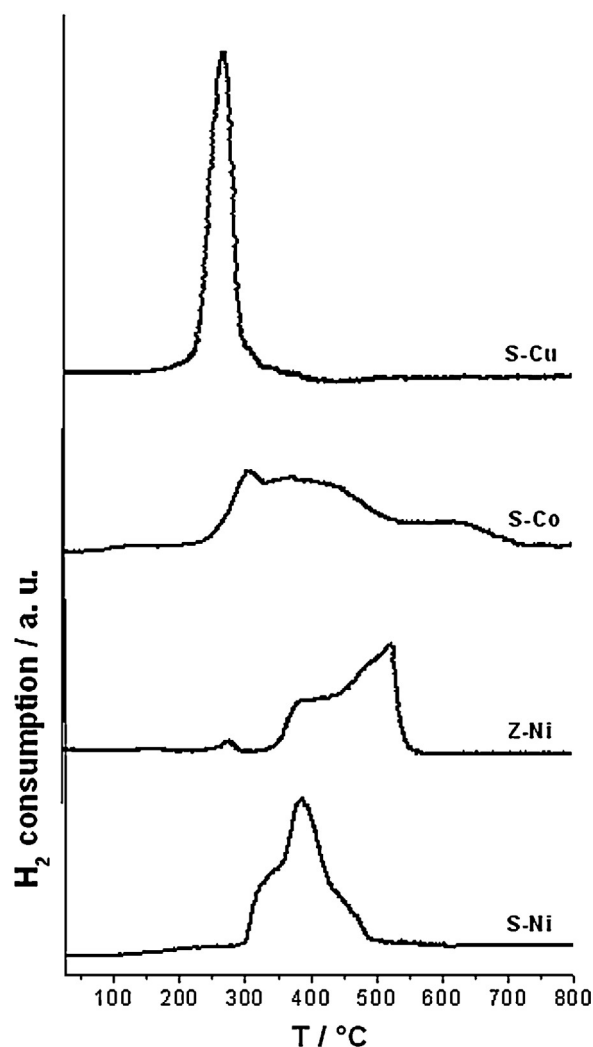


Fig. 1. TPR patterns of samples (a) S–Ni; (b) Z–Ni; (c) S–Co and (d) S–Cu.

NiO has a reduction temperature of about 280 °C [33]. The other two peaks can be assigned to NiO particles weakly or strongly interacting with the support (peaks at intermediate and high temperature, respectively). It can be noticed that the temperature of such peaks differs according to the nature of the support.

The TPR of sample S-Co (Fig. 1c) indicated broad and overlapping peaks, which may be attributed to the progressive reduction of Co^{3+} to Co^{2+} and of Co^{2+} to Co^0 [34–37]. The complete reduction of this metal oxide was achieved at higher temperature with respect to NiO reduction. By contrast, Cu, as expected, was the most reducible metal, catalyst S-Cu (Fig. 1d) revealing a single peak at 260 °C, corresponding to the one-step reduction of CuO to metallic Cu [38].

By comparing the two Ni-based samples, as previously recalled, a higher reducibility is usually ascribed to lower metal dispersion and *vice versa*. This hypothesis is supported by TEM micrographs reported in Fig. 2, which evidence a relatively broad particle size distribution for the SBA-15 supported sample (Fig. 2a), with particle size of the active phase ranging from 5 to 20 nm. Big crystals constitute the support, where the single particle domains were scarcely recognized. The SBA-15 porous structure was however evident. By contrast, much smaller particles of ZrO_2 , and hence of Ni (ca. 2–5 nm), were achieved with sample Zr-Ni (Fig. 2b), in agreement with TPR previsions. Bigger metal particle size was detected for S-Cu (Fig. 2c), whereas no well defined Co or CoO_x particles have been evidenced for sample S-Co.

XRD analyses of the as prepared samples were performed in order to identify the different phases present in the samples. Rietveld refinement was also done on most samples to quantify the content of each phase and to determine the crystal size.

The XRD pattern of sample S-Ni was collected at low angle (Fig. S1), revealing the mesoporous structure of the support. Similar patterns were collected also with samples S-Co and S-Cu. By contrast, the diffraction peaks obtained for the Zr-Ni can be mainly assigned to the tetragonal structure of ZrO_2 . Ni crystal size as determined by Rietveld analysis on the activated catalysts (reduced) was in agreement with TEM analysis. The trend of particle size of the active phase mimics that predicted by TPR, confirming that the biggest size is attributed to the most reducible sample, *i.e.* poorly interacting with the support, and *vice versa*.

Additional structural information may come from skeletal FT-IR spectra (not shown). The spectra of catalyst Zr-Ni indicated the presence of some monoclinic ZrO_2 (band at 745 cm^{-1}) together with the most abundant tetragonal phase, whose peaks are overlapped with monoclinic phase in the lower frequency region. The amorphous silica support was characterized by the typical absorption at 1078 cm^{-1} (with a shoulder at 1200 cm^{-1}), and by bands at 802 and 460 cm^{-1} due to stretching and deformation modes of the SiO_4 structural unit. A weak band at 962 cm^{-1} was assigned to Si-OH deformation modes. In a previous work, the presence of this band in the spectrum of silica supported Cobalt catalyst has been related to the interaction of Co oxides with the silica network: the higher the intensity of this band, the weaker the interaction of Co ions with the silica matrix [39]. The main IR bands detected for S-Cu were assigned to the lattice vibrational modes of the oxide support, nevertheless the presence of copper species in the form of copper oxides can be suggested by very weak bands around 600 cm^{-1} in the silica-based sample spectrum [40].

Spectra of the catalysts in the UV–vis NIR region are reported in Fig. 3. S-Co sample spectrum shows the formation of massive CoO_x species, characterized by broad absorptions at 415, 708 nm and 1360 and 1493 nm, consistent with the detection of the well defined IR features due to Co–O vibrational modes in the 650–550 cm^{-1} region of the IR skeletal spectrum (not reported). Possibly an amorphous phase of small cobalt oxide particles is formed, weakly interacting with the surface, not detectable by X-ray diffraction.

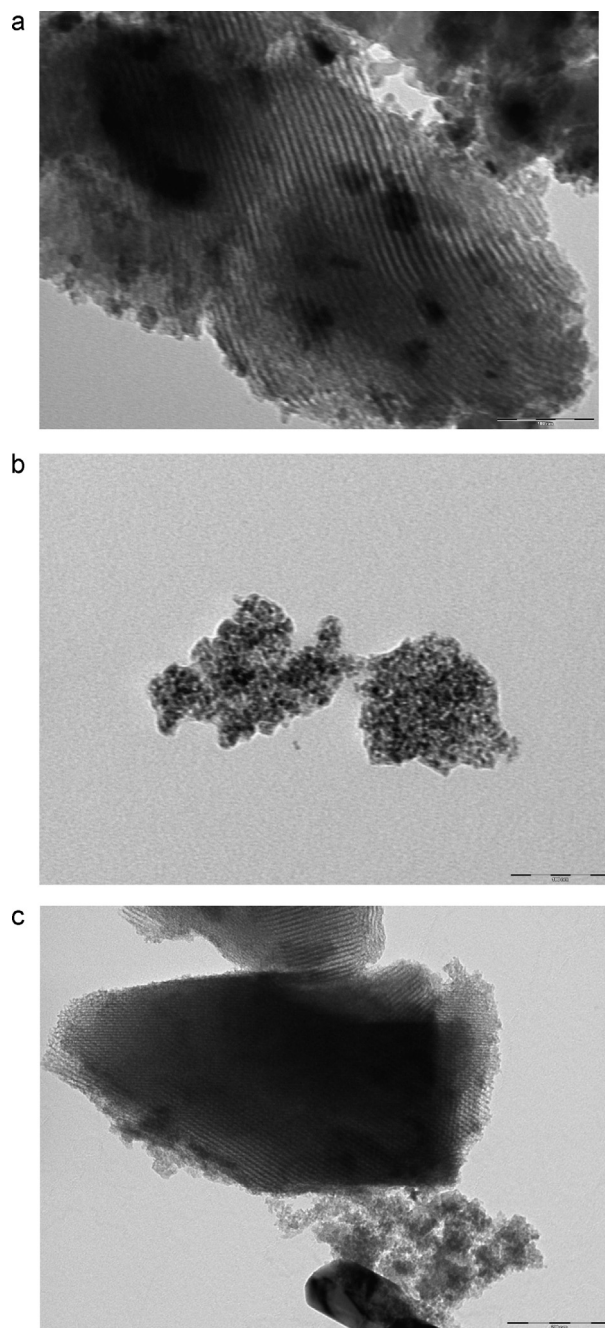


Fig. 2. TEM images of the fresh samples: (a) S-Ni; (b) Zr-Ni; (c) S-Cu. Marker size 100 nm for (a) and (b), 200 nm for (c).

The spectrum in the UV–vis–NIR region of sample Si-Cu shows only a strong and unstructured absorption extending in the visible region, which has been associated to the presence of large Cu metal particles [41], in perfect agreement with XRD and TEM data. In fact, according to literature, very large copper metal aggregates give rise to diffuse absorption without specific signals in electronic spectra [42].

The spectra of Ni-containing samples (both Zr-Ni and S-Ni) are consistent with spectra reported for similar materials, for instance the main complex absorption in the UV region, centred at ca. 280 nm, is due to electronic $\text{O}^{2-} \rightarrow \text{Ni}^{2+}$ charge transfer transitions and can be related to NiO dispersed phase and/or isolated Ni^{2+} ions. The same absorption appears slightly modified in the Zr-Ni

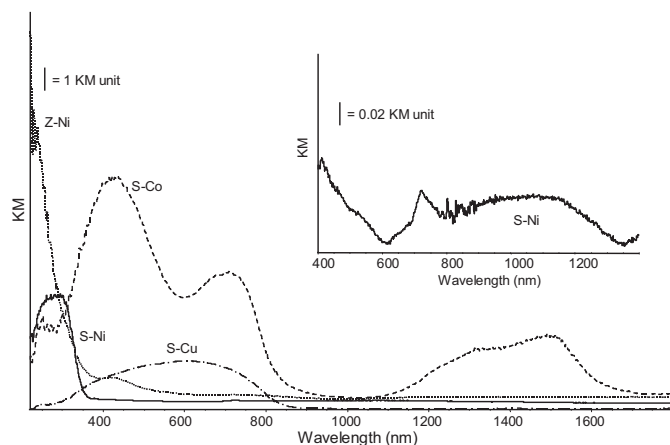


Fig. 3. DR-UV-vis NIR spectra of the catalysts.

spectrum, shifting to lower wavelength and increasing in intensity. This effect could be related to the different NiO particle size, which is slightly smaller in the Z-Ni sample. A weak peak at 720 nm, possibly with few minor components at lower frequencies, has been detected for the Si-Ni sample (see enlargement in Fig. 3) and assigned to d-d transitions of nickel ions [43]. These results are in agreement with the high dispersion of Ni^{2+} ions, since NiO small particles strongly interacting with the surface, as evidenced also by XRD and TPR data.

Summarizing, we can conclude that, in spite of the much higher surface area of the SBA-15 support, Ni is much more dispersed over ZrO_2 thanks to a stronger metal-support interaction. However, some more reducible species are also present. Cu gave rise to the biggest aggregates and did not evidence a significant interaction with the support. By contrast, Co was fairly good dispersed over silica and showed the less reducible metal oxide particles of this series.

3.2. FT-IR studies

Adsorption of CO (IR band in gas phase at 2138 cm^{-1}) is one of the most useful methods for characterizing the nature of dispersed transition metal species over catalytic surfaces [44]. Hence, we performed low temperature adsorption of CO over all the catalysts studied in order to investigate the redox state and morphology of metal particles. The most interesting results are reported and discussed in the following paragraphs.

Spectra of pure powder Z-Ni catalyst following activation at 500°C did not show bands characterizing zirconia isolated OH groups, but only a broad band of H-bound hydroxyl groups thus pointing out the strong perturbation of the support surface induced by Ni deposition (Fig. 4, inset). CO adsorption led to the detection of a broad band centred at 2180 cm^{-1} , with components at lower frequencies and assigned to CO coordinated over Zr^{4+} and possibly Ni^{2+} ions, forming carbonyls whose frequencies overlapped. This band decreased in intensity following outgassing and shifted to higher frequencies, in agreement to the strength of the surface sites. The shoulder at 2127 cm^{-1} can be attributed to the asymmetric stretching mode of a dicarbonyl complex of Ni^+ , whose corresponding symmetric stretching overlapped with the band at 2089 cm^{-1} . The former component readily disappears after a brief outgassing.

On the other hand, the high frequency band at 2089 cm^{-1} can be due to stretching mode of CO coordinated over Ni metal particles highly defective, thus on corner and edges sites, resending of a limited back-bonding effect from the metal particles.

The main band of this spectrum is centred at 2042 cm^{-1} thus in the typical frequency range of CO coordinated over Ni metal

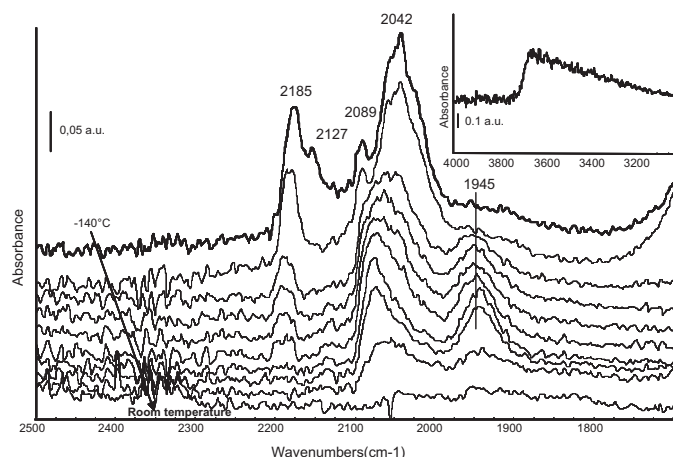


Fig. 4. FT-IR subtraction spectra of surface species arising from CO adsorption over Z-Ni catalyst at liquid nitrogen temperature and following outgassing upon warming. The activated surface has been subtracted. Inset: OH stretching region of the reduced surface.

particles [43]. Its quite low frequency should be explained by the increased back bonding effect from electron rich metal particles to CO anti-bonding orbitals. These results suggest that two type of Ni metal particles are formed at the Z-Ni catalyst surface, as evidenced also by TPR results: the first kind of particles (νCO at 2089 cm^{-1}) highly dispersed and strongly interacting with the surface, the second kind of particles (2042 cm^{-1}) characterized by a reduced interaction with the support. After outgassing upon warming, we observed significant changes in the spectra: the two bands merge in a broad absorption whose maximum shifted to 2080 cm^{-1} . Simultaneously, a component at 1945 cm^{-1} increased, pointing out that reconstruction phenomena occurred. As a consequence, two main carbonyl bands remained in the spectrum after outgassing, centred at 2080 and 1940 cm^{-1} : they were assigned to linear and bridging carbonyl species over regular metal particles, possibly coordinated over $\text{Ni}(100)$ and/or $\text{Ni}(111)$ planes [45]. This effect evidenced that the reconstruction phenomena mainly consisted in the coalescence of Ni metal particles, exposing flat surfaces, where bridging CO adsorption is favoured. The occurrence of some extended Ni particles upon activation or thermal treatment in the presence of a reducing agent such as CO may be consistent with the presence of highly reducible species as evidenced in the TPR pattern.

PN adsorption over the same catalyst (Fig. 5) led to the detection of a broad band at 2274 cm^{-1} , due to nitriles coordinated over exposed Zr^{4+} sites of medium acidic strength, pointing out that there is no evident effect of oxide deposition on surface acidity.

CO adsorption at 77 K over sample S-Ni (Fig. 6) gave rise to a main band at 2155 cm^{-1} , due to H-bound species, which corresponded to silanol negative band in the subtraction spectra (near 3600 cm^{-1} , not reported), and to a lower intensity band around 2134 cm^{-1} , due to liquid-like CO. As expected these bands readily disappeared upon outgassing. Bands at 2095 and 2050 cm^{-1} fall in the frequency region typical of CO adsorption on top of Ni metal particles, as discussed above. Moreover, the former band is quite complex and its component at the highest frequencies is also the most unstable upon outgassing, therefore it can be assigned to the symmetric stretching of nickel dicarbonyl species, i.e. $\text{Ni}^+(\text{CO})_2$. In this case the corresponding asymmetric stretching band should be detected, very weak, around 2130 cm^{-1} . CO adsorption nicely agrees with TPR results, which indicate the formation of different kinds of metal particles having different reducibility and, consequently, different interaction with the support.

After outgassing at increasing temperatures no reconstruction phenomena appear to modify the Ni metal particles: this means

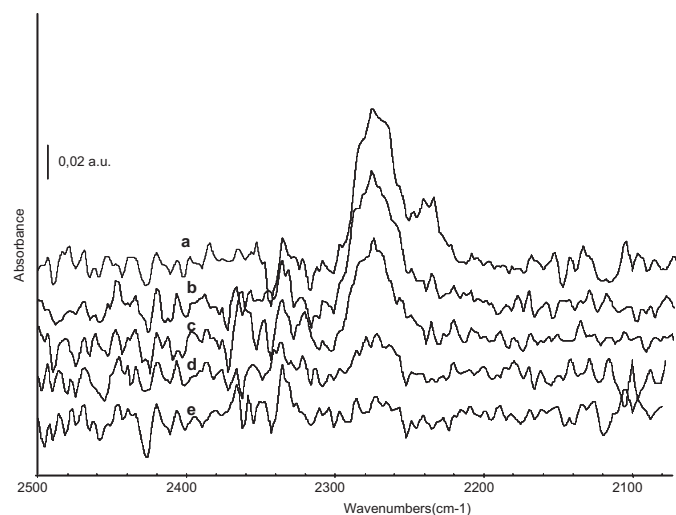


Fig. 5. FT-IR subtraction spectra of surface species arising from pivalonitrile (PN) adsorption over Z-Ni catalyst at room temperature (a); after outgassing at room temperature (b), after outgassing at room temperature for 30 min (c), at 150 °C (d) and 200 °C (e). The activated surface has been subtracted.

that at 500 °C all the reduction processes at the surface are completed leading to stable metal phase morphology.

PN adsorption led to a main band at 2245 cm^{-1} , due to PN H-bound to silanol groups of the silica support, as expected, whereas no bands due to PN coordinated over supported nickel oxide were detected (Fig. 7).

The spectra arising from CO adsorption over the sample S-Co are reported in Fig. S2. A main band is detected at 2155 cm^{-1} , readily disappearing upon warming. This feature is due to CO interacting with silanol groups of the support.

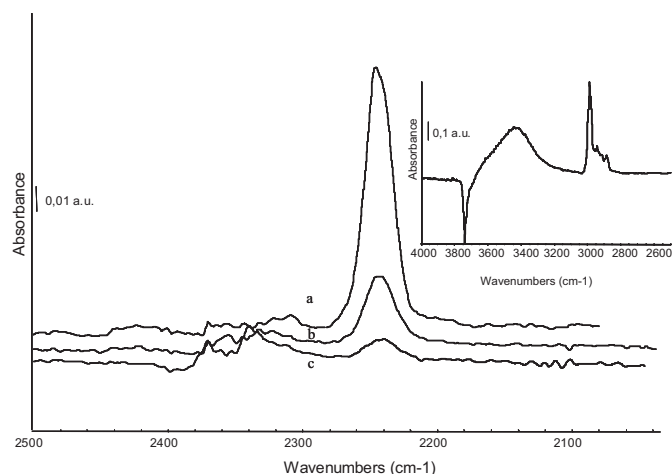


Fig. 7. FT-IR subtraction spectra of surface species arising from pivalonitrile (PN) adsorption over S-Ni catalyst at room temperature (a); after outgassing at room temperature (b), after outgassing at room temperature for 30 min (c). Inset: OH stretching region. The activated surface has been subtracted.

Bands at 2177 cm^{-1} (very weak) and 2136 cm^{-1} shifting towards lower frequencies (2120 cm^{-1}) are due to CO coordinated over a fraction of cobalt ions, which are not reduced by the mild reduction treatment applied in this experiment. On the other side, the spectra also show the presence of easily reduced Co ions. These are characterized by a complex carbonyl band centred at 2064 cm^{-1} and tailing towards lower frequencies. This is the frequencies range reported in the literature for CO coordinated over metal surface sites as $\text{Co}^0\text{-CO}$ or $\text{Co}^0(\text{CO})_n$, in agreement with TPR results which show the reduction of cobalt species to occur in a quite wide temperature range [46].

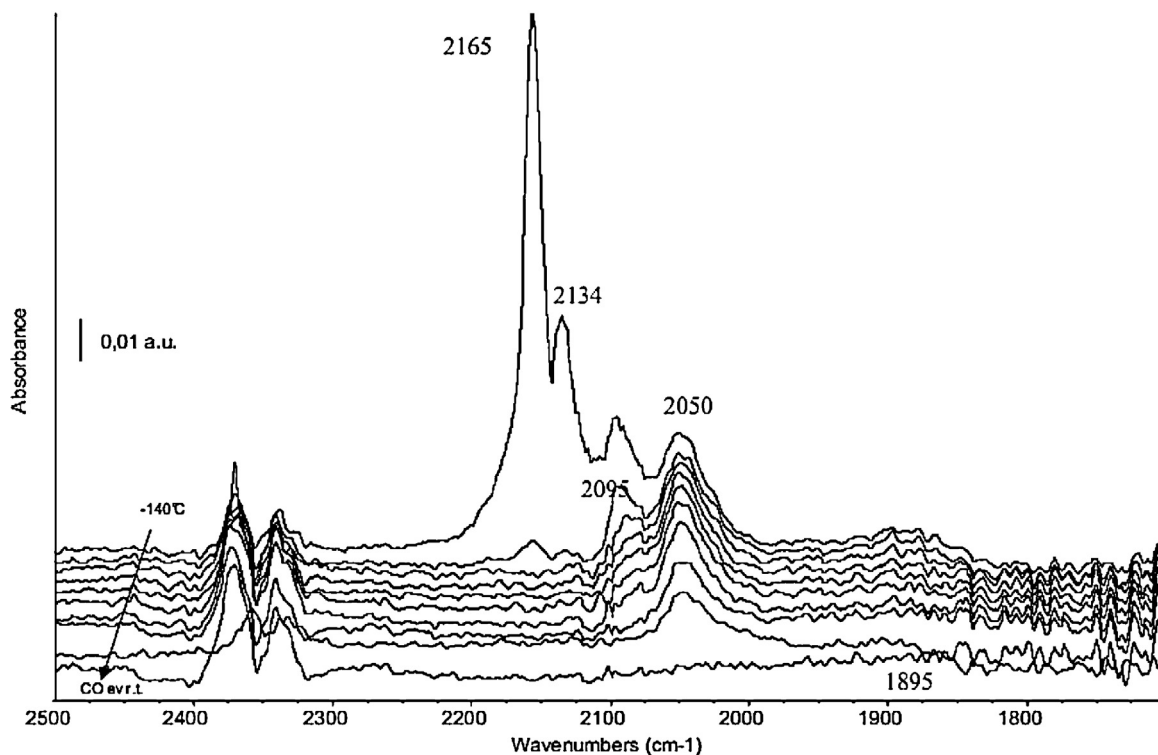


Fig. 6. FT-IR subtraction spectra of surface species arising from CO adsorption over S-Ni catalyst at liquid nitrogen temperature and following outgassing upon warming. The activated surface has been subtracted.

Table 2

Activity data for ESR at different temperature. GHSV = 1750 h⁻¹, P = 1 atm. Data averaged after 4–8 h-on-stream. For Z–Ni at 300 °C data collected up to 4 h-on-stream. Maximum theoretical productivity of H₂ per mol of ethanol fed: 4.1 at 500 °C, 1.8 at 400 °C and 0.6 at 300 °C [60].

500 °C	S–Ni	Z–Ni	S–Co	S–Cu
CO/CO ₂	0.58 ± 0.07	0.607 ± 0.018	0.78 ± 0.04	–
C balance (%)	105 ± 19 ^a	90.8 ± 1.1	93.4 ± 0.9	90 ± 2
Conv. H ₂ O	0.75 ± 0.04	0.54 ± 0.11	0.56 ± 0.04	0.56 ± 0.08
Conv. EtOH	1.00	1.00	1.00	0.12 ± 0.04
H ₂ productivity (mol/min kg _{cat})	1.3 ± 0.3	1.17 ± 0.02	0.950 ± 0.019	–
H ₂ /EtOH _{in} (mol/mol)	4.0 ± 0.7	3.47 ± 0.06	3.14 ± 0.06	–
S _{CH₃CHO} (%)	–	–	15.7 ± 0.6	46 ± 6
S _{CH₄} (%)	14 ± 4	18.7 ± 0.6	7.84 ± 0.17	–
S _{C₂H₂} (%)	–	–	5.4 ± 0.7	–
400 °C				
CO/CO ₂	0.97 ± 0.18	0.42 ± 0.07	1.07 ± 0.11	–
C balance (%)	73 ± 2	53 ± 5	98.3 ± 1.5	–
Conv. H ₂ O	0.78 ± 0.10	0.75 ± 0.11	0.542 ± 0.012	–
Conv. EtOH	0.79 ± 0.03	0.81 ± 0.06	0.282 ± 0.015	–
H ₂ productivity (mol/min kg _{cat})	0.50 ± 0.04	0.253 ± 0.006	0.133 ± 0.018	–
H ₂ /EtOH _{in} (mol/mol)	1.51 ± 0.12	0.75 ± 0.02	0.43 ± 0.05	–
S _{CH₃CHO} (%)	2.2 ± 0.2	7.2 ± 0.6	74 ± 4	–
S _{CH₄} (%)	23.1 ± 1.9	2.6 ± 0.3	3.25 ± 0.18	–
S _{C₂H₂} (%)	–	14.7 ± 1.0	–	–
300 °C				
CO/CO ₂	1.4 ± 0.2	–	–	–
C balance (%)	82 ± 2	74 ± 7	–	–
Conv. H ₂ O	0.814 ± 0.014	0.71 ± 0.05	–	–
Conv. EtOH	0.23 ± 0.03	0.27 ± 0.07	–	–
H ₂ productivity (mol/min kg _{cat})	–	–	–	–
S _{CH₃CHO} (%)	13.3 ± 1.3	100	–	–
S _{CH₄} (%)	3.6 ± 0.4	–	–	–
S _{C₂H₂} (%)	–	–	–	–

^a Value mediated between 1–8 h-on-stream. Values fluctuating from 79 to 128%, indicating partial self cleaning for S–Ni.

Finally, CO adsorption over reduced S–Cu sample gives rise mainly to a strong IR band at 2155 cm⁻¹ due to CO interacting with silanol groups (Fig. S3). Carbonyl species coordinated over residual Cu²⁺ ions are characterized by bands in the range 2180–2150 cm⁻¹, thus can be masked by the strong absorption of H-bound CO [47–49]. Following outgassing, all these bands disappear almost immediately, confirming their assignation to species weakly bound. The weaker component at 2133 cm⁻¹ is due to CO over residual oxidized copper Cu⁺ species. The shoulder at 2117 cm⁻¹, tailing towards lower frequencies, can be assigned to carbonyls over dispersed Cu metal particles. All these components are very labile and their thermal behaviour allow their assignation to reduced copper species, although the frequency range of these bands is unusually high [50].

CO and PN adsorption, studied by FT-IR spectroscopy, allowed the following remarks: over the nickel-based catalysts, after reduction in hydrogen at 500 °C, a quite heterogeneous population of metal species was detected in perfect agreement with the reducibility scale evidenced by TPR. Silica support seems to stabilize the nickel metal phase in two kinds of metal particles, in spite of the quite low calcination temperature. On the contrary, zirconia support allows the reconstruction of nickel species under CO adsorption, in spite of its ionic character and Lewis acidity, which should favour dispersion and stabilization of the supported oxide phase. Over silica several cobalt species available for CO coordination are formed. Medium Lewis acidity due to exposed support ions was detected over the zirconia-based catalyst, whereas over the silica-based ones Lewis acidity could only be induced by the metal phase itself, if any.

3.3. Activity testing for ESR

The activity of each sample was tested at 500 °C for the ESR reaction and the results are reported in Table 2 as average between 4 and 8 h-on-stream. This temperature was chosen as interesting

benchmark because it would allow to decrease the heat input to the reactor with respect to common operating conditions found in the literature ($T > 650$ °C). Furthermore, it allows to put in light possible deactivation phenomena related to coking. The latter is indeed particularly critical at this temperature since CO disproportion, ethanol dehydration to ethylene and its further polymerization may be active, but the possibly formed coke cannot be readily gasified by steam, particularly when a stoichiometric water/ethanol feeding ratio is adopted.

Full ethanol conversion was achieved for every sample except S–Cu, confirming the lower activity of Cu as active phase due to limited ability in C–C bond cleavage [51]. Indeed, this sample was selective mostly to acetaldehyde. The highest H₂ productivity was achieved with S–Ni, together with the smallest selectivity to methane, the only by-product obtained with Ni-based catalysts. By contrast, some C₂ products (acetaldehyde and ethylene) were observed for sample S–Co. In general, the performance of the present Co-based sample is less promising than what reported by other research groups for low-temperature steam reforming [52,53].

One of the most important parameters is C balance, which is helpful to understand if some coking is occurring over catalyst surface. The blank test at 500 °C, i.e. under the same reaction conditions but without catalyst, was characterized by ca. 91% C balance, due to C accumulation over the quartz beads filling the reactor. The results reported in Table 2 confirm this set of samples as very interesting from the point of view of their resistance to coking. Indeed, in every case the C balance was comparable to that of the blank test, excluding significant coke deposition over the catalyst bed, at least at this temperature.

A peculiar behaviour was observed with sample S–Ni, which exhibited C balance higher than 100% if averaged out after 4 h-on-stream (Table 2). Its profile (Fig. 8) suggested carbon accumulation during the first hours-on-stream, followed by its progressive gasification, corresponding to a sort of self-cleaning action. This is

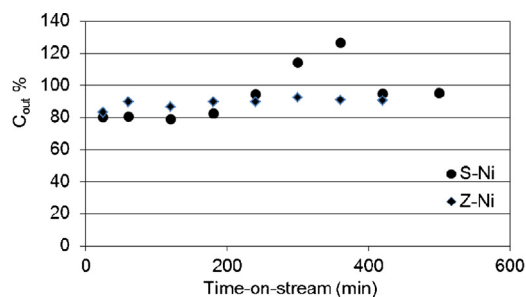


Fig. 8. Carbon balance vs. time-on-stream for samples S-Ni and Z-Ni at 500 °C.

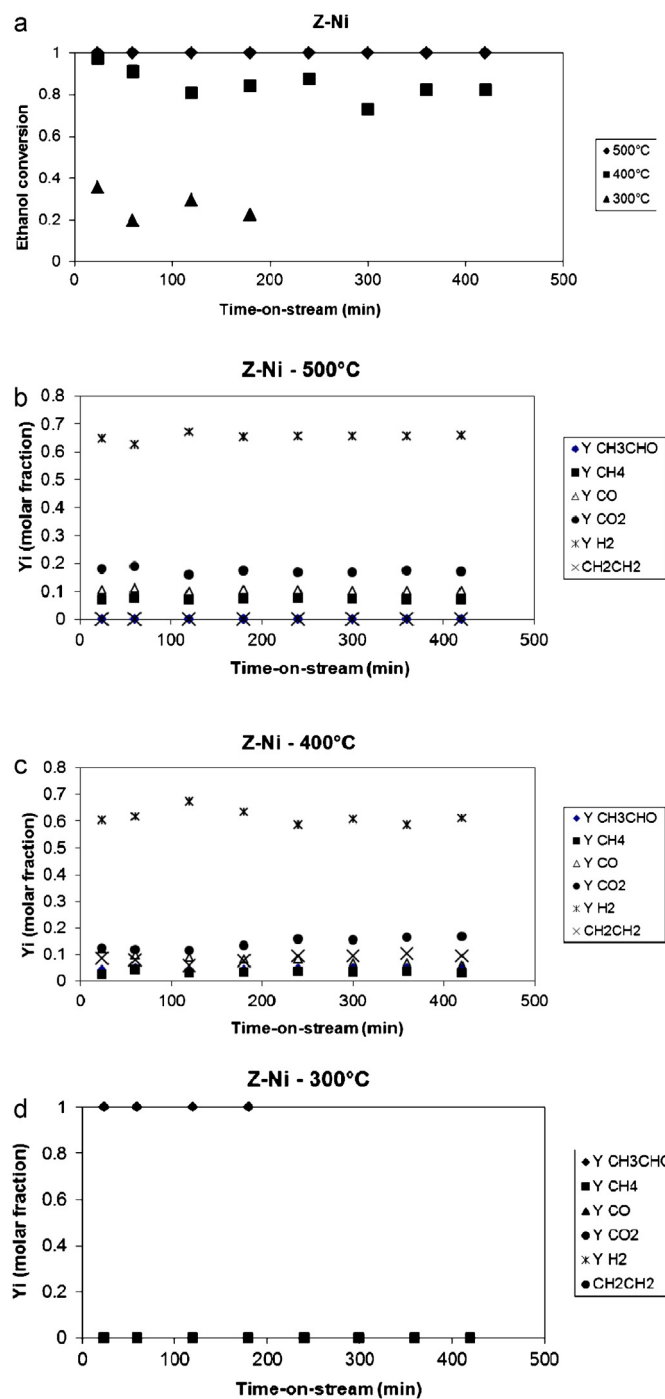


Fig. 9. Catalyst performance vs. time-on-stream of sample Z-Ni at different temperature. (a) Ethanol conversion; (b–d) product distribution in the outlet gas at 500, 400 and 300 °C, respectively.

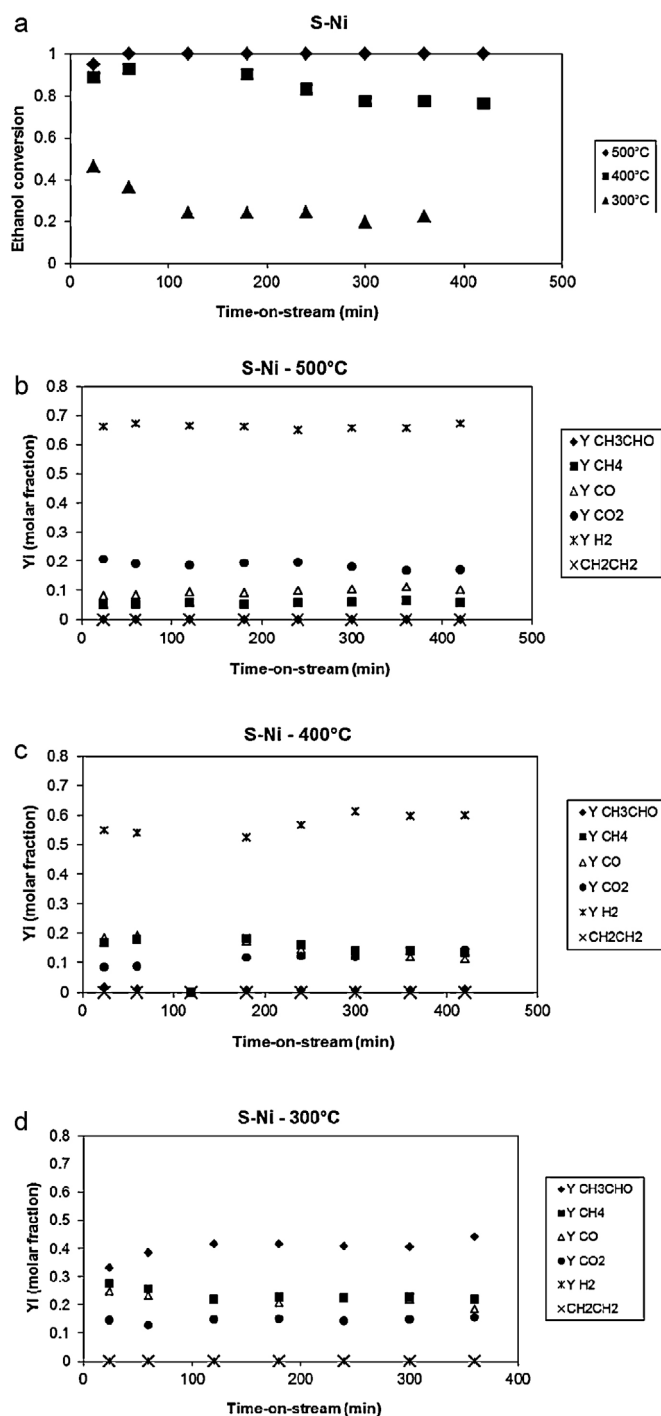


Fig. 10. Catalyst performance vs. time-on-stream of sample S-Ni at different temperature. (a) Ethanol conversion; (b–d) product distribution in the outlet gas at 500, 400 and 300 °C, respectively.

supported also by the highest average conversion of water. This self cleaning action has not been observed for sample Z-Ni, which on the contrary exhibited a rather stable C balance (Fig. 8).

These results rule out severe deactivation by coking at 500 °C, at least for the duration of the test. The supports, characterized by mild (ZrO₂) or nil (SiO₂) Lewis acidity (see FT-IR data) do not seem to contribute to coke deposition by polymerization of ethylene, typically favoured by strong acid sites. Therefore, if ethylene forms by ethanol dehydration, as in the case of S-Co, it does not accumulate over the catalyst in polymeric form at 500 °C.

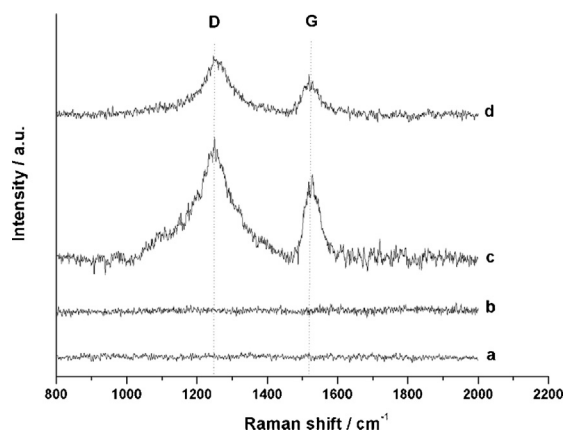


Fig. 11. Micro-Raman analysis of spent catalysts, (a) S–Ni, (b) S–Cu, (c) S–Co and (d) Z–Ni. The characteristic D and G bands of carbon nanotubes are evidenced.

The formation of carbon nanofilaments has been also reported over Ni particles, especially for bigger particle size [15–18]. Higher Ni dispersion has been observed for the fresh Z–Ni than for S–Ni, predicting in principle lower formation of C filaments for the former than for the latter, which additionally showed a bit broader Ni particle size distribution. Indeed, during the first h-on-stream the C balance was higher for sample Z–Ni than for sample S–Ni. Likely, C accumulation occurred over the biggest Ni particles for sample S–Ni, subsequently gasified until a steady state condition was reached. The smaller particles actually remained active, since no loss of activity with time-on-stream occurred.

On the basis of the interesting performance reached at 500 °C, we lowered the reaction temperature to 400 °C. Ethanol conversion dropped to less than 30% for S–Co, which exhibited very low H₂ productivity and selectivity mostly to acetaldehyde. Therefore, for both Co and Cu active phases, the main reaction path seems dehydrogenation of ethanol, as stated also elsewhere [54,55]. By contrast, both the Ni-based catalysts were still sufficiently active (ca. 80% ethanol conversion). Ethanol conversion and product distribution

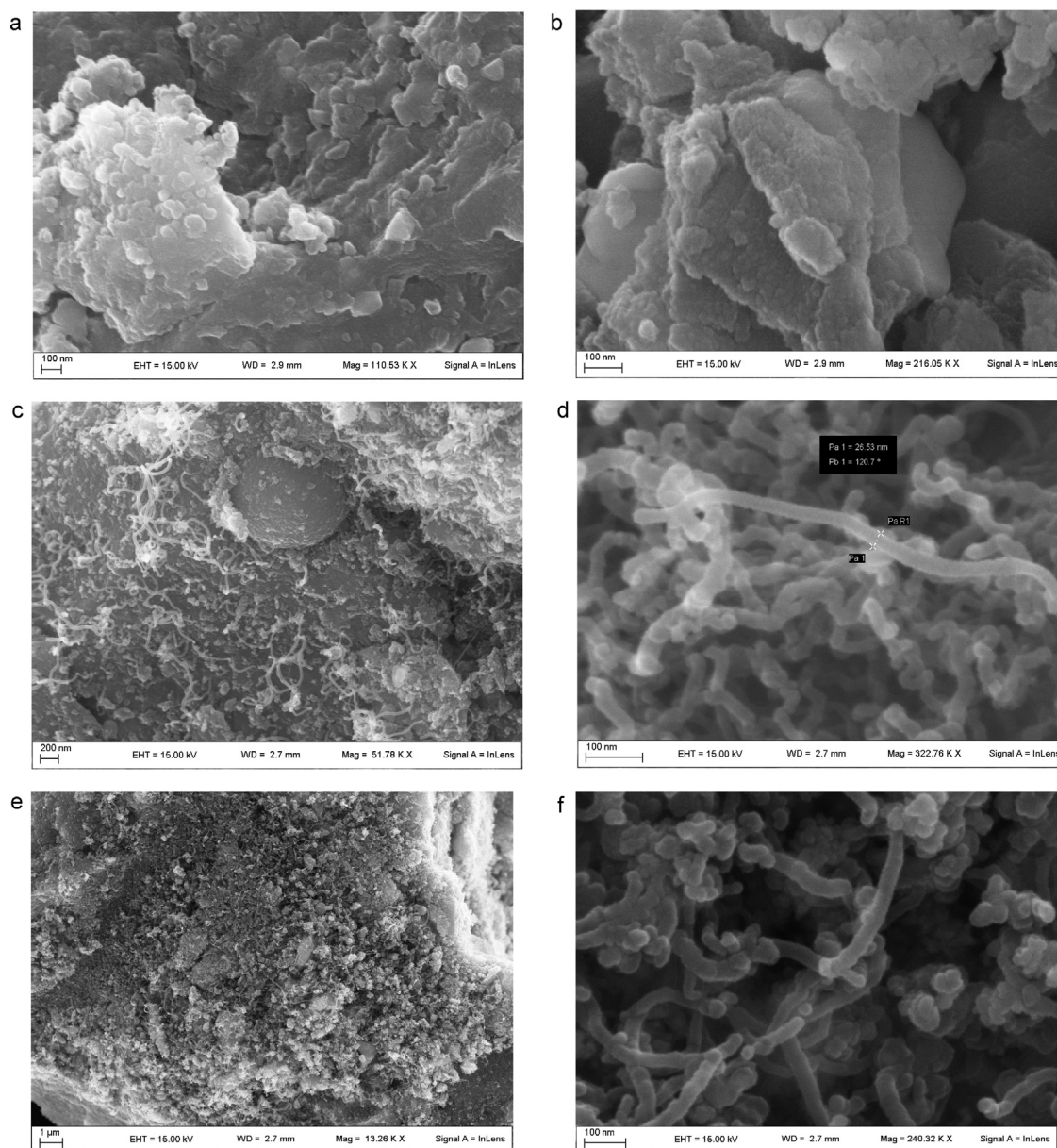


Fig. 12. FE-SEM analysis of the spent catalysts: (a) S–Ni; (b) S–Cu; (c and d) S–Co; (e–f) Z–Ni.

at different temperature vs. time-on-stream are summarized in Figs. 9 and 10. Sample S–Ni showed the highest C balance and CH₄ as main byproduct, insufficiently reformed at this temperature, whereas Z–Ni also formed some ethylene and acetaldehyde. These catalysts promoted different reaction paths, since that supported over SiO₂ was able to sustain ethanol decomposition, forming CH₄. By contrast, the ZrO₂-supported catalyst was not able to effectively activate the C–C bond, mainly leading to C₂ by-products. The very low C balance of Z–Ni, together with its non negligible selectivity to ethylene also suggests significant coke deposition over it at 400 °C. Nevertheless, its performance with time-on-stream remained rather stable (Fig. 9a and c). This suggests that coke accumulation did not affect significantly the active phase and thus it was likely due to polymerization over the Lewis acidic sites of the support.

An attempt to further lower reaction temperature down to 300 °C evidenced once again a similar ethanol conversion of both the Ni-based catalysts (below 30%). However, the ZrO₂-supported sample confirmed unable to promote ethanol reforming, being selective for its dehydrogenation to acetaldehyde, only. Furthermore, Z–Ni progressively deactivated with time-on-stream (ethanol conversion from 26 to 22% after 3 h-on-stream, Fig. 9a and d), whereas S–Ni kept a stable ethanol conversion (ca. 23%) for the whole duration of the test (Fig. 10). Moreover, by looking at the C balance, one may argue additional coking, especially for sample Z–Ni, possibly favoured by the reconstruction of the surface metal phase (as detected by FT IR). In this case coking is correlated to activity decrease, suggesting a progressive deactivation of the active phase.

3.4. Characterization of the spent catalysts

In order to better interpret activity data, particularly regarding resistance to coking, we characterized the spent catalysts by means of TPO, Micro-Raman, FE-SEM and TEM analyses. The catalysts were analyzed after reaction at the minimum temperature reported in Table 2, i.e. after testing at 500 °C for S–Cu, 400 °C for S–Co and 300 °C for S–Ni and Z–Ni.

No evidence of the typical Raman bands attributable to the formation of C nanotubes (CNTs) was observed for samples S–Ni and S–Cu (Fig. 11). By contrast, the D and G bands of CNTs appeared with samples S–Co and Z–Ni. FE-SEM (Fig. 12) and TEM (Fig. 13) analyses confirmed this attribution, evidencing in particular the presence of multi-walled CNTs in much higher concentration for S–Co than for Z–Ni. C accumulated over the samples was also quantified by TPO. The rate of C deposition was 18.8 mg C/g_{cat} h after testing at 300 °C of sample Z–Ni (10.2 mg C/g_{cat} h after testing at 500 °C as reported in [56]) and 8.1 mg C/g_{cat} h after testing at 500 °C for sample S–Co. This result should be coupled with the lower concentration of CNTs evidenced by TEM for Z–Ni than for S–Co. This confirms that the main coking mechanism for S–Co is the formation of CNTs. Additional coking may occur for Z–Ni due to support acidity in form of polymeric C (higher C accumulation, but lower formation of CNTs), which does not cover the active phase, thus not leading to activity loss at higher temperature.

Both Ni and Co are reported as catalysts for the formation of CNTs [57–59]. It is also known from the abundant literature on CH₄ reforming that smaller Ni particles are less prone to coking than bigger ones. The reason of such behaviour should be searched in the mechanism of coke formation over Ni [15–17]. The growth of carbon nanofibers in such case involves methane adsorption on the surface and its conversion into adsorbed carbon [18]. Then, carbon segregates into the layers near the surface by diffusion through Ni and precipitation on the rear side of the Ni crystal. Small Ni crystal size results in a large saturation concentration leading to a low driving force for carbon diffusion and hence a lower coking rate.

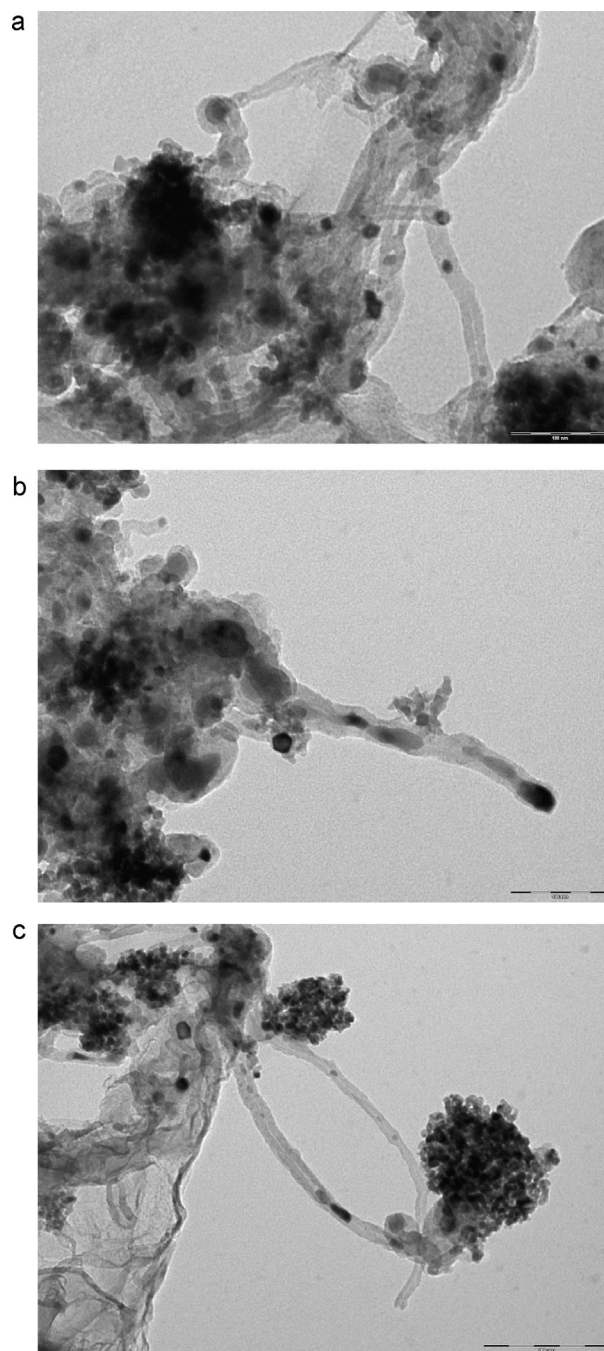


Fig. 13. TEM images of spent samples: (a) S–Co; (b and c) Z–Ni. Marker size = 100 nm for (a) and (b), 200 nm for (c).

In previous investigations we confirmed the positive effect of small Ni particle size on coking inhibition also for the steam reforming of ethanol [12] and glycerol [13].

Broad particle size distribution has been observed for Co in the spent S–Co catalyst, with the active phase often entrapped in CNTs (Fig. 13a). By contrast, the particle size of Ni in the spent sample Z–Ni showed much less uniform than for the fresh catalyst. Ni supported over ZrO₂ proved very active and resistant to coking when tested at 500 °C in a previous investigation [12,13]. However, in such case, the calcination at 800 °C during the synthesis procedure allowed to strengthen the metal–support interaction, leading to a more poorly reducible catalyst, where Ni was very well dispersed over the support and stabilized for high temperature use. In the present case, the particle size of the support remained

roughly constant after use at 500 °C for sample Z–Ni and most Ni particles were well dispersed as well, but accompanied by much bigger particles, as confirmed by IR results. The latter likely formed by sintering of the most reducible species evidenced by TPR (*i.e.* poorly interacting with the support) and seem the main responsible of CNTs formation (Fig. 13b and c). By contrast, the smallest Ni particles, remaining almost unaffected by thermal treatment and activity testing, were also free from carbon deposits.

Of course, the effect of acidity should be also taken into account, leading to additional coke deposition over the support acid sites (Z–Ni), which does not interfere with catalytic activity.

4. Conclusions

A set of catalysts for the ESR has been prepared with variable support (ZrO₂ and a mesoporous SiO₂) and active phase (Ni, Co, Cu). The present data confirm Ni-based ones as the most promising catalyst for this reaction at 500 °C. Indeed, full ethanol conversion was achieved, with satisfactory C balance, stable performance and limited formation of byproducts. Different reaction paths have been observed (*i.e.* different byproducts) depending on the active phase, but also on the support. In particular Co and Cu were predominantly active for ethanol dehydrogenation. The reforming activity for the conversion of acetaldehyde was very poor, whereas Co was able to convert it at least at 500 °C. However, by decreasing temperature poor activity was achieved. By contrast, both the Ni-based catalysts were active also at very low reaction temperature (300 °C). If at 500 °C the performance of the silica and zirconia-based catalysts is very similar, at lower temperature by-products started to form with Z–Ni, mainly related to its acidity (ethylene). Accordingly, some coking was observed, but not leading to catalyst deactivation, thus mainly ascribed to coke deposition over acidic sites. Therefore, acidity control plays a key role for low temperature testing.

By further decreasing temperature carbon accumulation was additionally due to the formation of carbon nanotubes over Ni. Metal dispersion confirmed a key role from this point of view. Both Co and Ni led to the formation of CNTs, but in the latter case this phenomenon was tightly dependent on the support and its interaction with the active phase. The strongest the metal–support interaction, evidenced by a lower reducibility of the metal ions, the highest the resistance to coking, mainly due to smaller Ni particle size.

Acknowledgements

The authors are indebted with Regione Lombardia and the Consortium for Material Science and Technology (INSTM) for financial support. The valuable help of Dr. Cesare Biffi and Matteo Compagnoni is gratefully acknowledged. The authors are indebted with Prof. Giuseppe Cruciani for XRD analyses. The work was partly supported by H2FC European Infrastructure Project (Integrating European Infrastructure to support science and development of Hydrogen and Fuel Cell Technologies towards European Strategy for Sustainable Competitive and Secure Energy), project reference 284522.

Appendix A. Supplementary data

Supplementary data associated with this article can be found, in the online version, at <http://dx.doi.org/10.1016/j.apcatb.2013.12.012>.

References

- [1] M. Barroso, A.E. Galletti, M.C. Abello, *Appl. Catal. A* 394 (2011) 124.
- [2] M. Benito, R. Padilla, A. Serrano-Lotina, L. Rodríguez, J.J. Brey, L. Daza, *J. Power Sources* 192 (2009) 158.
- [3] S.Q. Chen, Y. Liu, *Int. J. Hydrogen Energy* 34 (2009) 4735.
- [4] L.J.I. Coleman, W. Epling, R.R. Hudgins, E. Croiset, *Appl. Catal. A* 363 (2009) 52.
- [5] A.C. Furtado, C.G. Alonso, M. Pereira, N.R.C. Fernandes-Machado, *Int. J. Hydrogen Energy* 34 (2009) 7189.
- [6] P. Panagiotopoulou, D.I. Kondarides, X.E. Verykios, *Ind. Eng. Chem. Res.* 50 (2011) 523–530.
- [7] A.A.A. da Silva, L.O.O. da Costa, L.V. Mattos, F.B. Noronha, *Catal. Today* 213 (2013) 25–32.
- [8] L.V. Mattos, G. Jacobs, B.H. Davis, F.B. Noronha, *Chem. Rev.* 112 (2012) 4094–4123.
- [9] A.N. Fatsikostas, X.E. Verykios, *J. Catal.* 225 (2004) 439–452.
- [10] F. Díaz Alvarado, F. Gracia, *Chem. Eng. J.* 165 (2010) 649.
- [11] A. Lima da Silva, C. de Fraga Malfatti, I.L. Muller, *Int. J. Hydrogen Energy* 34 (2009) 4321.
- [12] I. Rossetti, C. Biffi, C.L. Bianchi, V. Nichele, M. Signoretto, F. Menegazzo, E. Finocchio, G. Ramis, A. Di Michele, *Appl. Catal. B: Environ.* 117–118 (2012) 384.
- [13] I. Rossetti, A. Gallo, V. Dal Santo, C.L. Bianchi, V. Nichele, M. Signoretto, E. Finocchio, G. Ramis, G. Garbarino, A. Di Michele, *ChemCatChem* 5 (2013) 294.
- [14] E. Finocchio, I. Rossetti, G. Ramis, *Int. J. Hydrogen Energy* 38 (2013) 3213.
- [15] G. Centi, S. Perathoner, *Catal. Today* 148 (2009) 191.
- [16] V.M. Gonzalez-Dela Cruz, J.P. Holgado, R. Pereniguez, A. Caballero, *J. Catal.* 257 (2008) 307.
- [17] K.O. Christensen, D. Chen, R. Løding, A. Holmen, *Appl. Catal. A* 314 (2006) 9.
- [18] D. Chen, K.O. Christensen, E. Ochoa-Fernandez, Z. Yu, B. Tødtal, N. Latorre, A. Monzón, A. Holmen, *J. Catal.* 229 (2005) 82.
- [19] Z. He, M. Yang, X. Wang, Z. Zhao, A. Duan, *Catal. Today* 194 (2012) 2.
- [20] E. Ghedini, M. Signoretto, F. Pinna, G. Cruciani, *Catal. Lett.* 125 (2008) 359.
- [21] V. Nichele, M. Signoretto, F. Menegazzo, A. Gallo, V. Dal Santo, G. Cruciani, G. Cerrato, *Appl. Catal. B: Environ.* 111–112 (2012) 225.
- [22] F. Zane, S. Melada, M. Signoretto, F. Pinna, *Appl. Catal. A: Gen.* 299 (2006) 137.
- [23] *Selected Powder Diffraction Data*, Minerals, vol. 1, DBM, JCPDS, Swarthmore, PA, 1974–1992, pp. 40.
- [24] S. Brunauer, P.H. Emmett, E. Teller, *J. Am. Chem. Soc.* 60 (1938) 309.
- [25] E.P. Barrett, L.G. Joyner, P.P. Halenda, *J. Am. Chem. Soc.* 73 (1951) 373.
- [26] S. Subramanian, *Platinum Metal Rev.* 36 (1992) 98.
- [27] S.J. Tauster, S.C. Fung, R.L. Garten, *J. Am. Chem. Soc.* 100 (1978) 170.
- [28] S.J. Tauster, *Acc. Chem. Res.* 20 (1987) 389.
- [29] B. Huang, X. Li, S. Ji, B. Lang, F. Habimana, C. Li, *J. Nat. Gas Chem.* 17 (2008) 225.
- [30] S. Ren, P. Zhang, H. Shui, Z. Lei, Z. Wang, S. Kang, *Catal. Commun.* 12 (2010) 132.
- [31] Y.Q. Song, D.H. He, B.Q. Xu, *Appl. Catal. A* 337 (2008) 19.
- [32] V. García, J.J. Fernández, W. Ruiz, F. Mondragón, A. Moreno, *Catal. Commun.* 11 (2009) 240.
- [33] L. Zhang, J. Lin, Y. Chen, *J. Chem. Soc., Faraday Trans.* 88 (1992) 2075.
- [34] B. Jongsomjit, T. Wongsalee, P. Praserttham, *Catal. Commun.* 6 (2005) 705.
- [35] S. Sun, N. Tsubaki, K. Fujimoto, *Appl. Catal. A* 202 (2000) 121.
- [36] F. Boubekr, A. Davidson, S. Casale, P. Massiani, *Microporous Mesoporous Mater.* 141 (2011) 157.
- [37] S.S. Reddy, B.D. Raju, A.H. Padmasri, P.K.S. Prakash, K.S.R. Rao, *Catal. Today* 141 (2009) 61.
- [38] E.M. Fixman, M.C. Abello, O.F. Gorris, L.A. Arrua, *Appl. Catal. A* 319 (2007) 111.
- [39] S. Esposito, M. Turco, G. Ramis, G. Bagnasco, P. Pernice, C. Pagliuca, M. Bevilacqua, A. Aronne, *J. Solid State Chem.* 180 (2007) 3341.
- [40] J.A. Gadsden, *Infrared Spectra of Minerals and Related Inorganic Compounds*, Butterworths, Reading, MA, USA, 1975.
- [41] F. Boccuzzi, S. Coluccia, G. Martra, N. Ravasio, *J. Catal.* 184 (1999) 316.
- [42] A.N. Pestryakov, V.P. Petranovskii, A. Kryazhov, O. Ozhereliev, N. Pfänder, A. Knop-Gericke, *Chem. Phys. Lett.* 385 (2004) 173.
- [43] G. Garbarino, S. Campodonico, A. Romero Perez, M.M. Carnasciali, P. Riani, E. Finocchio, G. Busca, *Appl. Catal. A: Gen.* 452 (2013) 163.
- [44] K. Hadjiivanov, G. Vayssilov, *Adv. Catal.* 47 (2002) 307–511.
- [45] K. Coulter, X. Xu, D.W. Goodman, *J. Phys. Chem.* 98 (1994) 1245.
- [46] A.Y. Khodakov, J. Lynch, D. Bazin, B. Rebours, N. Zanier, B. Moisson, P. Chaumette, *J. Catal.* 168 (1997) 16–25.
- [47] G. Busca, *J. Mol. Catal.* 43 (1987) 225.
- [48] A. Dandekar, M.A. Vannice, *J. Catal.* 178 (1998) 621.
- [49] A. Gervasini, M. Manzoli, G. Martra, A. Ponti, N. Ravasio, L. Sordelli, F. Zacheria, *J. Phys. Chem. B* 110 (2006) 7851.
- [50] K. Hadjiivanov, T. Tsoncheva, M. Dimitrov, C. Minchev, H. Knözinger, *Appl. Catal. A: Gen.* 241 (2003) 331.
- [51] R.R. Davda, J.W. Shabaker, G.W. Huber, R.D. Cortright, J.A. Dumesic, *Appl. Catal. B: Environ.* 56 (2005) 171.
- [52] L. Chen, C.K.S. Choong, Z. Zhong, L. Huang, Z. Wang, J. Lin, *Int. J. Hydrogen Energy* 37 (2012) 16321.
- [53] M. Domínguez, E. Taboada, E. Molins, J. Llorca, *Catal. Today* 193 (2012) 101.
- [54] I.V. Deinega, L.Yu. Dolgikh, I.L. Stolyarchuk, L.A. Staraya, P.E. Strizhak, E.M. Moroz, V.P. Pakharukova, D.A. Zyuzin, *Theor. Exp. Chem.* 48 (2013) 386.
- [55] I. Rossetti, J. Lasso, E. Finocchio, G. Ramis, V. Nichele, M. Signoretto, A. Di Michele, *Appl. Catal. A: Gen.* (2013), submitted for publication.
- [56] V. Nichele, M. Signoretto, F. Menegazzo, I. Rossetti, G. Cruciani, G. Cerrato, *Appl. Catal. B* 150–151 (2014) 12–20.
- [57] M. Natha, B.C. Satishkumara, A. Govindaraja, C.P. Vinoda, C.N.R. Rao, *Chem. Phys. Lett.* 322 (2000) 333.
- [58] D.S. Bethune, C.H. Clang, M.S. de Vries, G. Gorman, R. Savoy, J. Vazquez, R. Beyers, *Nature* 363 (1993) 605.
- [59] S. Kurasawa, S. Iwamoto, M. Inoue, *Mol. Cryst. Liq. Cryst.* 387 (2002) 123.
- [60] G. Rabenstein, V. Hacker, *J. Power Sources* 185 (2008) 1293–1304.